Cobble motion characterisation with smart sensors through laboratory experiments for ground-based landslide monitoring

Abstract

Landslides often contain boulders on their surface or within the landslide body. Embedding sensors inside boulders within a landslide may help monitor its movement and dynamics. In this study, smart sensors were tested for tracking movements of a cobble, estimating its magnitude and mode of movement in dedicated laboratory experiments. The cobble was embedded with a sensor equipped with accelerometers, gyroscopes, and magnetometers. The experiments consisted of letting the cobble travel down an inclined plane. By changing the angle of the inclined plane, the cobble showed different modes of movement such as rolling and, when embedded in a thin sand layer, sliding. While travelling down the slope, the cobble was tracked to infer its position from camera videos. Raw sensor data were used for motion detection and discerning the mode of movement. Sensor-based acceleration and camera-based position were fed to a Kalman filter to derive the cobble velocity and compute the total kinetic energy to characterise the motion magnitude. Furthermore, LoRaWAN wireless transmission was tested by burying the cobble in sand layers of different thickness. The experiments contributed to understanding how the sensor functions and may be applied in the field for landslide monitoring, modelling and early warning systems.

Non-technical Summary

Landslides often transport boulders and cobbles either on their surface or embedded within the landslide body. Thus, tracking the motion of boulders and cobbles can provide information about the movement of the landslide in which they are embedded. Smart sensors were inserted into a cobble and were rolled down an experimental hillslope in a laboratory. By letting the cobble fall on an inclined plane tilted at different angles, the sensor tracked different types of cobble movement (namely rolling and sliding). . The experiments were recorded by a camera placed at the end of the experimental table. The ability of the sensor to transmit data wirelessly from inside a landslide was tested separately by burying the cobble at different depths in a sand filled bucket. The results demonstrate how smart sensor data can separate between rolling and sliding, approximate the energy of movement and send data remotely when buried in a layer of sand. The trials helped to clarify how sensors work and guide the use of sensors on real landslides for monitoring and early warning of landslide hazards.

Keywords

Boulders, laboratory experiments, smart sensors, landslide, ground monitoring

1 Introduction

Under climate change, precipitation has increased in intensity and frequency making landslide events more likely (e.g., Gariano and Guzzetti, 2016; Auflič et al., 2023). Rapid urbanization and demographic growth have made more people vulnerable to landslide hazards especially in low -income countries (e.g., Pollock and Wartman, 2020) leading to the development of different approaches in landslide risk management (e.g., Sim et al., 2022). Slow-moving landslides occur on high slopes and are typically sensitive to seasonal rainfall given their clay rich texture and complex subsurface network (e.g., De Blasio, 2011; Lacroix et al., 2020). Usually, these systems approach catastrophic collapse by progressively increasing displacement or alternating phases of stability and movement, either seasonal or annual (e.g., Crosta et al., 2017; Chang and Wang, 2022). In many field applications, the rate of change of displacement can be used to reliably anticipate the time of failure (Carla' et al., 2017; Intrieri et al., 2019; Leinauer et al., 2023). Satellite remote sensing techniques such as InSAR can be used to monitor displacement and aid prediction of catastrophic failure of slow-moving landslides but are limited to several days in temporal resolution and hindered by dense vegetation (e.g., Dini et al., 2020; Mondini et al., 2021; Handwerger et al., 2022). Traditional ground-based methods of monitoring slow moving landslides (e.g., piezometers, extensometers, inclinometers, time-domain reflectometry) provide valuable and precise information in specific locations, but they are more expensive than remote sensing as they require drilling and often complex installation (e.g., Auflič et al., 2023). More recently, Passive Radio Frequency Identification (RFID) tags have been installed in boulders to track their displacements (e.g., Le Breton et al., 2019, 2022). These tags provide information about the movements with low battery consumption (Le Breton et al., 2019). However, all these ground-based techniques tend to be interrupted, damaged or destroyed by the landslide motion they are trying to capture.

While moving, landslides erode debris from hillslopes such as boulders and cobbles that can remain embedded in the body of the landslide while being transported downslope (e.g. Shobe et al., 2020, 2021). Recent advances in Micro-electromechanical systems (MEMS) have allowed the development of compact (few millimetres) and affordable sensors that can measure different environmental features with low power consumption offering new opportunities to effectively monitor stability of boulders embedded in landslides (e.g., Dini et al., 2021; Wang C. et al., 2022). When used in combination with a wireless network and with the appropriate firmware and hardware, the sensors become smart, i.e. they have the ability to provide an accurate and automated collection of environmental data. In summary, these sensors could be relatively small in size, low in price and versatile in the application and hence show a multifaceted potential.

Smart sensors were deployed previously in the field to collect data on rock falls (Niklaus et al., 2017; Caviezel et al., 2018, 2019, Coombs et al., 2020; Souza and Benoit, 2024). More recently, boulders embedded in the body of a landslide have been used not only in the study of landform shape and evolution, but also in hazard assessment where they can be employed to measure slope-based displacement (Bennett et al., 2016; Shobe et al., 2020; Dini et al., 2021; Shobe et al., 2021; Roskilly et al., 2022, 2023). Sensors embedded in boulders start recording when movement is detected due to rotations or impacts exceeding a custom-defined threshold. Furthermore, smart sensors were used in laboratory experiments to study energy dissipation in pebble-bed collisions (Peng et al., 2024) or track pebbles embedded in a granular flow for motion characterisation (Gronz et al., 2016; Dost et al., 2020). In this case, accelerometers, gyroscopes, and magnetometers were installed within five pebbles released in a flume. Although the granular flow was completely contained within the flume, some of the pebble trajectories inferred from sensor data were out of range, appearing to fall outside of the flume walls, indicating inability of sensors alone to reliably represent pebble motion and the need for further research (Dost et al., 2020).

The essential feature that makes sensors smart is their integration within a network that sends data to a server via wireless communication (e.g., Dini et al., 2021), i.e. a Wireless Sensor Network (WSN). The development in the Internet of Things (IoT) and Wireless Sensor Networks (WSN) have made possible the remote communication amongst sensors in the network and between the sensing network and servers (e.g., Gronz et al., 2016; Mao et al., 2019; Hart and Martinez, 2020; Dini et al., 2021). In geomorphology applications, MEMS are usually equipped with a transceiver and antenna to send data (e.g., Maniatis et al., 2021). Recent studies have made use of LoRaWAN, a wireless communication protocol capable of long distance and low power data transfer (Dini et al., 2021; Roskilly et al., 2022, 2023). Before applying this technology to landslide monitoring, LoRAWAN technology had given positive outcome to send data from motion sensors in wild animal tracking (e.g. Soriano-Redondo et al., 2021; Gauld et al., 2023). Communication is bidirectional, permitting the sensor to both send data and receive messages in return. Once motion is recorded, data are stored and transmitted to receivers via LoRaWAN. Finally, the data are transmitted to cloud storage via the internet, usually using cellular networks. Thus, LoRaWAN wireless transmission represents an advance over RFID sensors where communication is only one-way and over shorter distances. However, the use of LoRaWAN as protocol to send data from motion sensors has not yet received much attention in geomorphology.

These recent applications highlight that the reliability of these sensors still need to be evaluated for monitoring purposes and tested for the development of early warning systems. The present study aims to improve our understanding of the functioning of motion sensors and LoRaWAN transmission protocol and to test their use in dedicated laboratory experiments before their deployment in ground-based monitoring in landslide settings. Specifically, a tag equipped with accelerometers, gyroscopes and magnetometers was tested to get insight on how to discern mode of movements, and capture magnitude of motion of a single cobble travelling down a slope. The sensor was tested over different slope inclinations and modes of movement. The LoRaWAN wireless data transmission was also tested through sand layers of different thickness to study the impact on the signal strength received from the sensor. The study is organised as follows. The experimental setup, the sensor details and the experimental campaigns are described in Section 2. Then, the results from LoRaWAN data transmission tests and the findings on raw and processed data for cobble motion are shown in Section 3. Finally, the insights gained from the experiments and on how this can improve the application of this technology in ground-based monitoring of boulders are discussed in Section 4.

2 Materials and Methods

2.1 Experimental setup

The experimental setup shown in Figure 1a consisted of an inclined panel (1500 mm x 1500 mm), followed by a horizontal one (2000 mm x 1500 mm) as in Manzella et al. (2016) and Makris et al. (2024). At the upper end of the inclined plane, a glass box with a sluice gate was installed to hold and release the cobble (Figure 1a). To control the spreading of the run out when the cobble is embedded in a sand layer, two acrylic side walls were mounted on the table constraining the maximum spread to

30 cm. A GoPro HERO8 located at the end of the horizontal board was used to record the experiments (Figure 1a). To track moving objects, the GoPro camera was set at 4K resolution with linear distortion and a frame rate of 30 fps. Further details about camera tracking are in the Supplementary Material. The cobble used in the experiments has an approximately round shape (Figure 1b and c). On the vertical plane the cobble had a diameter of 10 cm, whereas on the transversal plane, the cobble diameter was around 8 cm (Figure 2a and b). The cobble had a cylindrical borehole with a diameter of 4 cm and a depth of 7.5 cm (Figure 1b and c). The hollowed cobble was made of concrete cast using a mould created from a real cobble (further details on cobble making are in Clark, 2023). A smart sensor was placed within the borehole to detect the movements of the cobble (Figure 2a, b, and c). Specifically, the smart sensor used was a Miromico-manufactured device (Miromico manual, 2020a, b) equipped with a 9-axis sensor comprising accelerometers, gyroscopes, and magnetometers (ST LSM9DS1) powered by a 3.6 V lithium thionyl chloride battery. The device is equipped with an additional low-power 3-axis accelerometer sensor (ST LIS2DH) used to continuously monitor acceleration. When the movement exceeds the user-defined threshold (configured to 390 mg in this study), the continuously monitoring accelerometer wakes the 9-axis sensor that begins recording. The smart sensor is also provided with LoRaWAN for wireless communication and a microcontroller to regulate data acquisition, processing, and transmission. The sensors in the LSM9DS1 record with their maximum range, i.e. the accelerometers at ±16g, the gyroscopes at ±2000 °/s, and the magnetometer at ±16 Gauss. The sensor tag and the battery were placed within a sensor enclosure stuffed with cotton-pads to damp and prevent overload damage due to violent impacts (Figure 2b). The sensor enclosure was then inserted into the cobble so that the sensor tag sat at the bottom of the borehole. The upper part of the cavity was then sealed with a blue tack for a total weight of 0.7 kg (Figure 2c). Although the cotton pad buffer in the sensor enclosure does not ensure a fixed sensor installation position within the cobble and can increase the error in the measurements, it is necessary to prevent damage to the sensor by dampening the impact overload and preserving the integrity of the sensors (Feng et al., 2023). This has been taken into account when analysing the data.

The recorded data can be wirelessly transferred to a cloud server for online retrieval using a LoRaWAN gateway, or it can be manually downloaded via a USB cable. A Dragino-manufactured gateway was used for the tests and placed 3 m from the experimental table (Dragino LPS8 manual, 2021). The OpenWRT-based gateway is powered by an open-source software, with minor customisations of the stock firmware applied for additional features such as remote access and cellular modem support. The network was composed of the sensor, an end-node device, and the LoRaWAN gateway. The LORIOT network server receives the data from the gateway and then relays it to the SENSUM cloud server (Roskilly et al., 2022, 2023). Besides the transmitted data, LORIOT provides each transmission with received signal quality metrics, namely the Received Signal Strength Indicator (RSSI) and the Signal-to-Noise Ratio (SNR). The signal strength that the gateway receives from the end node is measured by RSSI, which typically falls between -120 dBm and -30 dBm, indicating a weak reception and a high reception, respectively. SNR is defined as the ratio of the power of the received signal to the power of the background signal noise. SNR levels are typically between -20 dB and 10 dB, with higher values indicating less corrupted signal. MEMS features are summarized in Table 1.

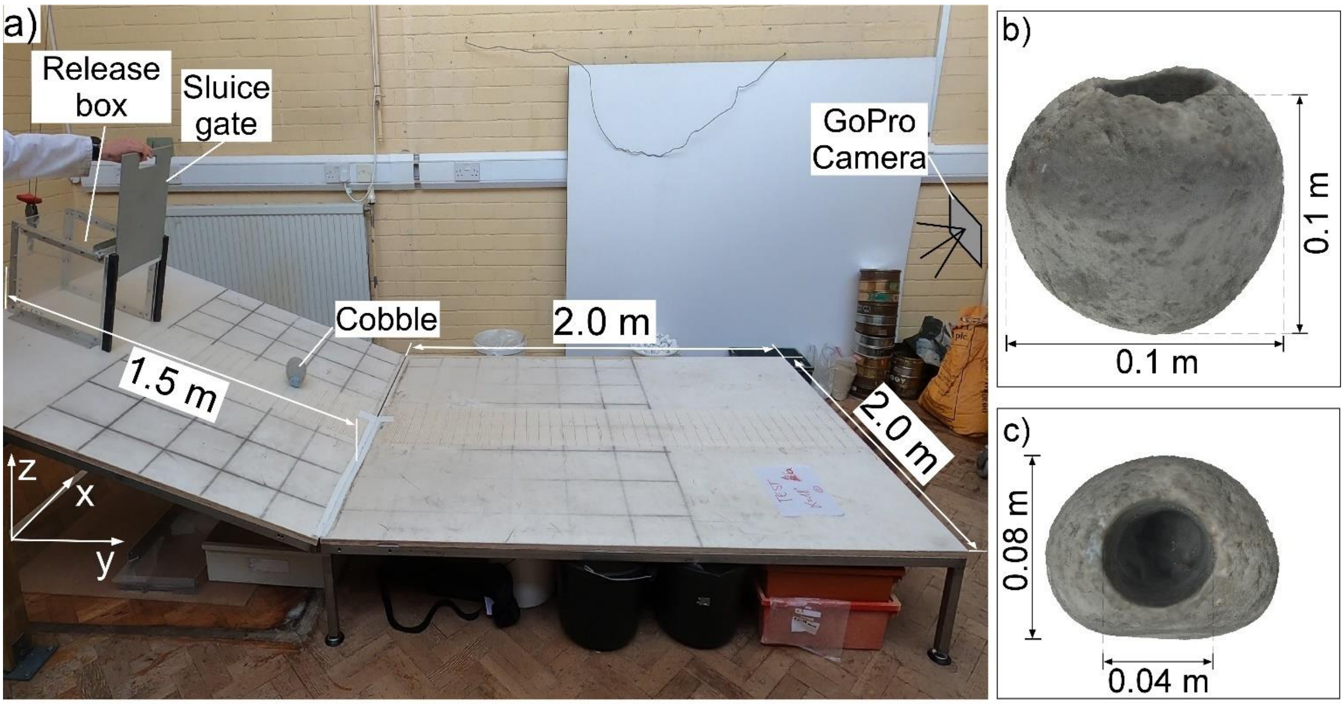

Figure 1 Experimental setup as in Manzella et al. (2016) and Makris et al. (2024). (a) Lateral view of experimental table. b), c) Cobble used in the experiments (Clark, 2023).

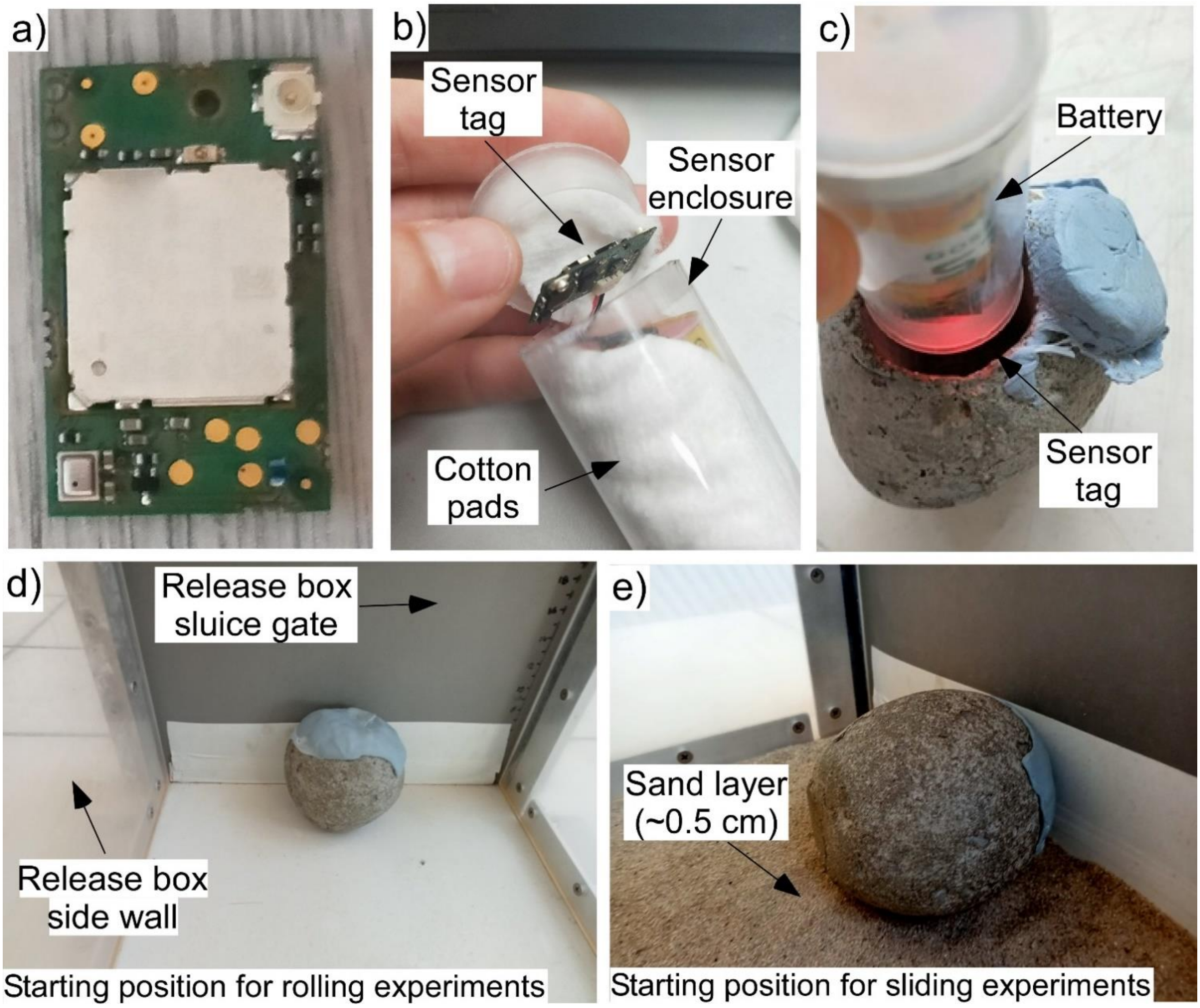

Figure 2 Laboratory experiments pictures. a) Sensor tag. b) and c) Sensor installation in the cobble. The starting position of the cobble within the release box for (d) rolling experiments and (e) sliding experiments while embedded in a thin layer of sand.

Table 1. Main sensor parametric features (Miromico manual, 2020a, b).

MEMS	
Power supply	3.6 V battery
3-axis sensor (ST LIS2DH)	2 Hz
Parameter	
Accelerometers	±2g
Acquisition frequency	2 Hz
Acceleration threshold to wake 9-axis sensor	390 mg
9-axis sensor (ST LSM9DS1)	
Parameter	
Accelerometers	±16 g
Gyroscopes	±2000 °/s
Magnetometers	±16 Gauss
Acquisition frequency (Accelerometers, Gyroscopes)	14.9 Hz or 59.5 Hz
Acquisition frequency (Magnetometers)	5 Hz
LoRaWAN	
Parameter	
Received Signal Strength Indicator (RSSI)	from -120 dBm to -30 dBm
Signal-to-Noise ratio (SNR)	from -20 dB to 10 dB

2.2 Data-fusion approach

~~Micro-electromechanical systems (~~MEMS~~)~~ usually suffer from stochastic and deterministic errors, including bias, scale factor errors, misalignments, noise, latency, and temperature dependence (e.g., Dewhirst et al. 2016). These factors hamper tracking based on Inertia Measurement Unit (IMU) and magnetometer (i.e., inertial navigation or dead reckoning), which is detrimental to its use in position/velocity monitoring. To avoid these issues and harness the best information about object motion, it is necessary to fuse sensor data together and use the camera-based positions as movement constraints (e.g., Dewhirst et al. 2016). This data fusion approach can be summarised in five steps as illustrated in the flowchart in Figure 3.

First, the raw recordings are retrieved from the sensor at the end of each run. Second, calibrated data are derived from the sensor raw recordings. Magnetometers and each sensor in the Inertial Measurement Unit are calibrated. Specifically, the accelerometers are calibrated according to Frosio et al. (2009), the gyroscopes according to Glueck et al. (2013) and the magnetometers according to Dewhirst et al. (2016). Details on the calibration framework used are reported in the Supplementary Material. Third, the orientation is computed combining the readings of the accelerometers, gyroscopes, and magnetometers (e.g., Madgwick et al., 2011; Mahony et al., 2012). Here, the orientation is derived following the approach proposed in Mahony et al. (2012) coded in the AHRS (Attitude and Heading Reference System) python library (AHRS library, 2019). Fourth, linear accelerations were inferred from the accelerometers through gravity compensation. The fusion of these data sources eliminates the low frequency drift caused by integration of gyroscope errors, while giving better high frequency accuracy than accelerometer and magnetometer measurements alone. Then, given the sensor orientation (attitude) with respect to the local Earth reference frame, the calibrated accelerometer measurements are rotated from the local body reference frame to the local Earth reference frame using simple transformations. The last step in the pipeline for IMU and camera tracking data fusion is a linear Kalman filter fed by sensor-derived (linear) accelerations and camera-based positions (Dewhirst et al., 2016; Kim and Bang, 2019).

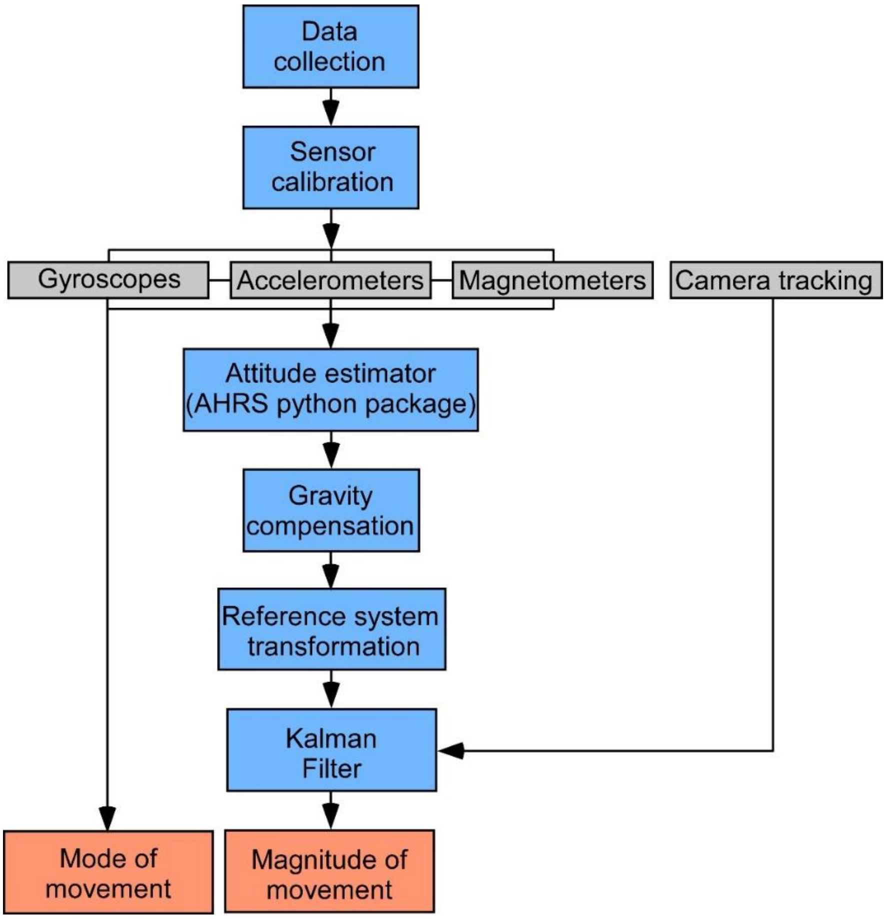

Figure 3 Pipeline for IMU and camera tracking data fusion. In short, the raw data retrieved from the sensors are calibrated following the procedure related to each sensor and then filtered to better describe cobble kinematics.

The sensors embedded in the cobble provide internally-measured acceleration data, that can be integrated for velocity and position change, but the derived data are prone to drift over time while the camera provides position data measured externally. Although camera-based position is subject to noise when differentiated for velocity and acceleration, it can constrain the drift from sensor data alone. By combining the measurement data, a two-step recursive algorithm computes the state of the system defined as the position, velocity, and linear acceleration of the cobble. The uncertainty in the state estimate is assessed by the relative weight given to the measurements and current state estimate. Additional information about sensor calibration and Kalman filter implementation can be found in the Supplementary Material.

2.3 Design of the experiments

Two experimental campaigns were conducted to test the performance of smart sensors in monitoring the movements of a cobble (Table 2). In the first set of experiments, the LoRaWAN wireless data transmission was tested using a gateway and a sensor acting as an end-node device. The experiments were carried out indoors with the gateway mains powered and the sensor battery powered. Specifically, to replicate the attenuation the terrain may exert on smart sensor transmitting data, the device was covered by sand layers of increasing thickness (namely 0 cm, 5 cm, 8 cm, and 10 cm) to measure the signal strength of data packets transmitted via LoRaWAN. The sensor was placed in a plastic box and buried in sand within a bucket ensuring that there was a minimum sand layer was achieved in all directions. By moving the bucket, the sensor then detected movement sending data to the gateway placed at a distance of 3 m. For these experiments, the acquisition frequency for the accelerometers and gyroscopes was set at 14.9 Hz, the magnetometers recorded at 5 Hz. In the second experimental campaign, the magnitude and mode of movements were analysed with the sensor installed in a cobble travelling down different inclines, namely 18°, 25°, 30°, 35°, 40°, 45°, 50° and 55°. The tagged cobble was placed within the release box with the sealed borehole facing upwards and a side leaning on the sluice gate (Figure 2f). The starting position allows the cobble to roll down the table. For slopes of 25° to 40°, the same experiments were also carried out embedding the cobble in a thin sand layer (~0.5 cm) to reduce the friction on the table and favour sliding motion. The cobble was placed within the release box with the sealed borehole leaning on the sluice gate (Figure 2g). The starting position of the cobble and the sand layer prevent full rotation and allows the cobble to slide down the table. For slope angles larger than 40°, sliding motion was not ensured and thus it was possible to carry out only rolling-type trials. Each run was repeated three times. For these movement experiments the acquisition frequency for the accelerometers and gyroscopes was set at 59.5 Hz and the magnetometers recorded at 5 Hz. In this set of experiments, the data were downloaded from the sensor via a USB cable. The raw data collected showed the cobble movements in space and time. To characterise the mode of movement for each inclination, a typical behaviour was inferred from the data following the procedure described. First, the vector magnitudes of the acceleration, angular velocity and the magnetic field data were computed. Second, each vector norm was averaged over the run duration. Then, error bars were computed from these averages. Finally, camera-based data and sensor-based data were filtered (Figure 3) to better describe cobble motion.

Table 1. Experimental campaigns. In the first experimental campaign, the sensor secured in a plastic box and buried under a sand layer of different thickness was moved so that Received Signal Strength Indicator (RSSI) and the Signal-to-Noise ratio (SNR) were sent to LORIOT network service through LoRaWAN. In the second experimental campaign, cobble motion down an inclined plane was tested for different mode of movements and slope inclination. Three repeats for each test were conducted (tick symbol stands for 3 repeats).

First experimental campaign: Testing LoRaWAN under sand layers	
Experiment series	**Sand layer thickness (mm)**
A	0
B	5
C	8
D	10
E	15

Second experimental campaign: Testing MEMS for cobble motion			
Experiment series	**Slope inclination**	**Rolling experiments**	**Sliding experiments**
F1	18°	✓	
G1	25°	✓	
G2	25°		✓
H1	30°	✓	

H2	30°		✓
I1	35°	✓	
I2	35°		✓
J1	40°	✓	
J2	40°		✓
K1	45°	✓	
L1	50°	✓	
M1	55°	✓	

3 Results

3.1 Received signal transmitted by LoRaWAN through sand

The power of the received sensor data transmissions was evaluated with two metrics, the Received Signal Strength Indicator (RSSI) and the Signal-to-Noise Ratio (SNR) (Figure 4). For the accelerometer and gyroscope data packets, the median value of RSSI is -35 dBm with no sand coverage (Figure 4a). The median value decreases to -45 dBm when sensors are submerged in a 10-cm sand layer. Moreover, the cumulative probability increases its slope suggesting data closely distributed around its median value. Similarly, the signal strength indicator of the magnetometer data packets is sensitive to sand layer depths (Figure 4b). Indeed, the median value RSSI decreases from -35 dBm to -55 dBm. In contrast with the behaviour of accelerometer and gyroscope packets, the cumulative probability becomes less tilted since the sample is more dispersed around the median. Overall, the RSSI is more sensitive to sand submergence with magnetometer data than with the gyroscope and accelerometer data. However, this sensitivity behaves differently. For the accelerometer and gyroscope packets, the RSSI becomes concentrated around the median value. On the other hand, for the magnetometer packets, differently from the gyroscope and accelerometer, RSSI is lower but more dispersed when the sensor is submerged in a sand layer probably due to a different acquisition frequency. Moreover, the SNR is not as sensitive as RSSI to sand layer submergence. SNR is positive ranging between 5.4 dB and 13.5 dB for the accelerometer and the gyroscope data packets (Figure 4c) and between 5.2 dB and 13.0 dB for the magnetometer data packets (Figure 4d). Regardless of the sand thickness tested, the median value for SNR stays approximately constant for both packet types.

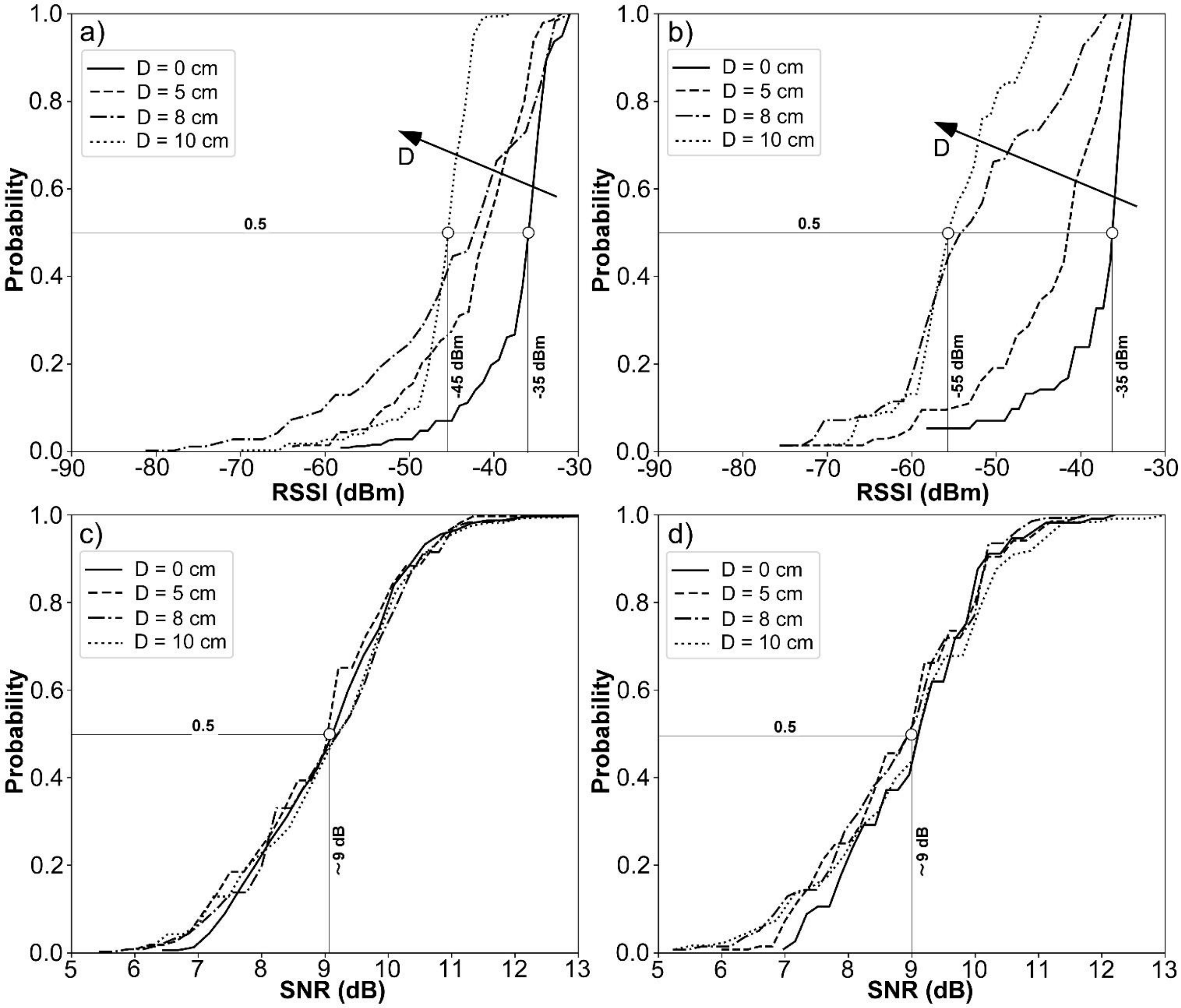

Figure 4. Cumulative probability distribution of (a and b) Received Signal Strength Indicator (RSSI) and (c, d) Signal Noise Ratio (SNR) when the signal is transmitted through different sand layer depths, namely 0 cm, 5 cm, 8 cm, and 10 cm (experiment series A-E, Table 2). RSSI and SNR are measurements of the signal power received in the gateway and the ratio of the signal power and the noise power, respectively. (a, c) Accelerometer and gyroscope packets. (b, d) Magnetometer packets.

3.2 Recordings from accelerometers, gyroscopes, and magnetometers and camera-based positions

Raw data recorded on a 30° incline are shown as an example of characteristic signals of the sensors while the cobble travels down the slope (Figure 5). Similar observations can be derived from the raw data collected on other slope angles. Sensor outputs show different ranges when the cobble freely travels down the tilt table (Figure 5a, b, c) compared to when it travels while embedded in a sand layer (Figure 5e, f, g). Following its release, the cobble was seen simply sliding down the incline when embedded in the sand, but without the sand it rolled down the table instead. These different modes of movement are evident in the gyroscope recordings. When the cobble is not embedded in a sand layer, the angular velocities increase progressively reaching maximum magnitude at the junction between the sloping and the horizontal board and then gradually decrease (Figure 5a). The angular velocities along all axes range between -2000 °/s and 1200 °/s, confirming the rolling movements seen in the experiments. Conversely, when the cobble is embedded in a sand layer, full rotations do not occur and thus the angular velocities show less variation, between -200 °/s and 400 °/s (Figure 5e). The smaller range for the angular velocities denotes a different behaviour, confirmed by the sliding observed during the experiment.

The accelerometer detects the impacts occurring during the motion. When the cobble rolls down the slope, the acceleration signal shows spikes across all axes representing the contact impacts between the cobble and the experimental table during the rolling motion (Figure 5f). The highest magnitude peaks occur when the cobble touches the horizontal board at the end of the sloping board and reaches the value of -14.5 g in the vertical direction. Conversely, when the cobble is embedded in a sand layer, the accelerometer signals are smoother ranging between –0.5 g and 2.0 g (Figure 5f). Accelerations in all directions show smaller changes with a small spike occurring when the slope becomes horizontal along the experimental table.

Magnetometer recordings exhibit some differences depending on the mode of movements. In the sliding experiment, the magnetic field signal is flat in all directions as the cobble travels down the slope and it changes slightly as the cobble slows down on the horizontal board (Figure 5g). Similarly, in the rolling experiments, while the cobble is on the slope, the magnetic field data are approximately constant with time and are then subject to larger variations when the cobble decelerates (Figure 5c). Between modes, some differences are seen in the magnetic field values, ranging between -0.5 and 0.5 Gauss for the rolling experiments and -0.2 and 0.6 Gauss for the sliding ones.

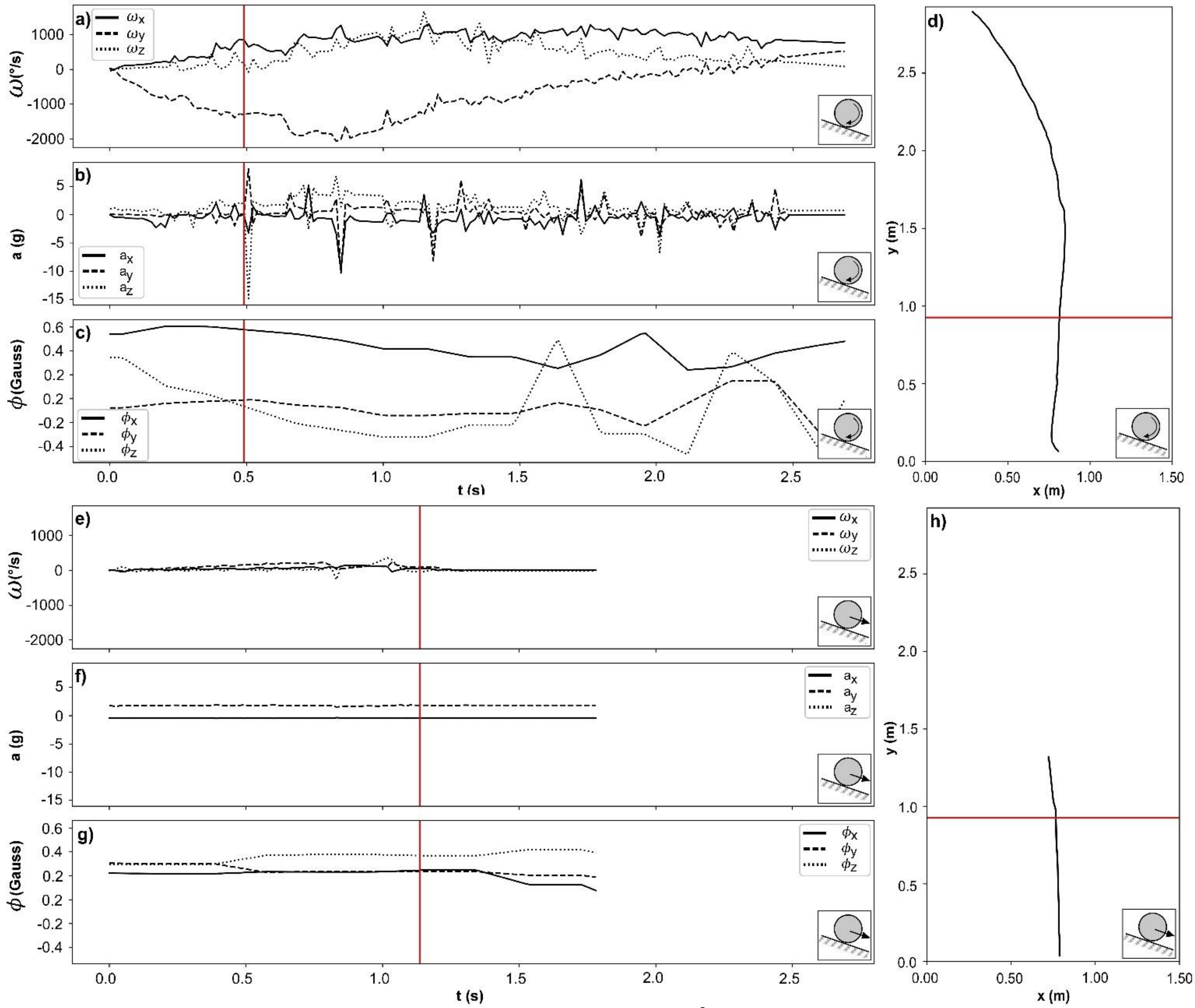

Figure 5. Raw recordings of the three sensor types on a 30° incline for (a, b and c) a rolling experiment (experiment series H1, Table 2) and (e, f and g) a sliding experiment (experiment series H2, Table 2). (a, e) gyroscopes data, (b, f) accelerometers data, (c, g) magnetometers data after upsampling. The solid line refers to the x axis, the dashed line to the y axis and the dotted line to the z axis. Trajectories extracted from camera videos for (d) rolling tests and (h) sliding tests carried out on a 30° incline. The solid red line shows the time when the cobble passes over the slope break.

The cobble paths tracked by the camera on the 30° incline are shown to highlight the differences between the rolling trajectory (Figure 5d) and sliding trajectory (Figure 5h). When the cobble is rolling, the trajectory keeps approximately straight and then, in the second half of the horizontal board, tends to drift to the left-hand side. These paths can be explained based on the momentum and the irregular shape of the cobble. After the release, the cobble accelerates rapidly increasing its momentum. Thus, along the slope, when the momentum is high, the cobble hardly drifts from its initial direction. At the junction between the slope and the horizontal board, the cobble keeps on rolling in the same direction without losing contact with the surface. In the second half of the horizontal board, when the momentum has reduced, the irregular shape of the cobble makes its trajectory drift. Conversely, when the cobble is embedded in sand, it keeps approximately the same side in contact with the experimental table and slides down the slope. Since full rotations do not occur, the irregularities on the cobble surface only slightly affect the trajectory so that it is approximately straight. On the horizontal board, the cobble motion is quickly stopped by the sand layer. Thus, the resulting trajectories are shorter than in the rolling experiments.

3.3 Lumped representation of motion from raw data

The cobble activity was lumped into error bars representing the spatiotemporal averages over all runs for each slope and for rolling and sliding experiments (Figure 6). In Figure 6, error bars on the left-hand side refer to motion on the inclined plane (Figure 6a, c, and e), and error bars on the right-hand side correspond to the motion on the horizontal plane (Figure 6b, d, and f). The error bars referring to the gyroscopes show a clear separation between rolling and sliding experiments from both the magnitude and distribution of angular velocity (Figure 6a, b). Specifically, sliding experiments exhibit similar values for angular velocity on the inclined plane (Figure 6a) and on the horizontal plane (Figure 6a) regardless of the slope angle ($\omega \approx 0^\circ$/s). Conversely, rolling experiments show different behaviour depending on inclination. On the inclined plane, the angular velocity becomes larger as the tilt table increases to 50° and then drops at a slope of 55° (Figure 6a). A similar trend is shown on the horizontal plane where the cobble released from a more inclined plane has larger values of angular velocity (Figure 6b). On the horizontal plane, at around 50°-55°, the increasing trend of angular velocity also shows a sudden drop on the horizontal plane. On both planes, the angular velocity for rolling experiments ranges between 1000 $^\circ$/s and 2500 $^\circ$/s.

Raw acceleration data shows a clear separation between rolling and sliding experiments (Figure 6c, d). This separation suggests a remarkable difference in the acceleration depending on the mode of movement, as the acceleration in sliding experiments (1-1.5 g) was smaller than in rolling experiments (namely 1.5-4.0 g). The sensor was not tightly fixed to borehole walls resulting in slight motion of sensor when the cobble travels down the incline, especially during full rotations. Hence, the vibrations were seemingly higher ~~than~~ in the rolling experiment rather than in the sliding experiments resulting in higher values of total acceleration. On the inclined plane, the acceleration does not increase with the slope inclination and shows an irregular trend. Specifically, the acceleration increases up to a 35° incline, then it decreases at 40°, it goes up again at 50° before dropping at 55°. On the horizontal plane, the acceleration in rolling experiments is more regular as the cobbles released from higher slopes show larger acceleration (Figure 6d). However, between 50° and 55°, the acceleration drops stopping the increasing trend. Although the raw acceleration magnitude and distribution separate the modes of movement, the irregular behaviour, especially for high slopes, is not completely clear from a physical point of view. Raw acceleration data need further investigation to explain the cobble dynamics on the slope.

Similarly, the raw magnetometer data show irregular behaviour. Magnetometer recordings have a similar range regardless of the mode of movements (Figure 6e, f). However, in the rolling experiments, the magnetic field magnitude decreases non-monotonically by increasing the inclination up to 35° on the inclined and the horizontal plane. For a slope of 40°, the magnetic field drops abruptly and then shows similar values for higher slopes on both the inclined and the horizontal plane. Conversely, in the sliding experiments, raw data increases with incline up to 35° and then it slightly decreases at 40°. Overall, the magnetic field magnitude changes non-monotonically for rolling and sliding experiments. However, in the rolling experiments, the magnetic field tends to decrease as the slope angle increases, whereas, in the sliding experiments, it has the opposite trend. The same behaviour is observed on both the horizontal and the inclined plane. Although different trend responses are seemingly detected for a slope increase, it is not possible to characterise the mode of movement with the magnetometer data alone.

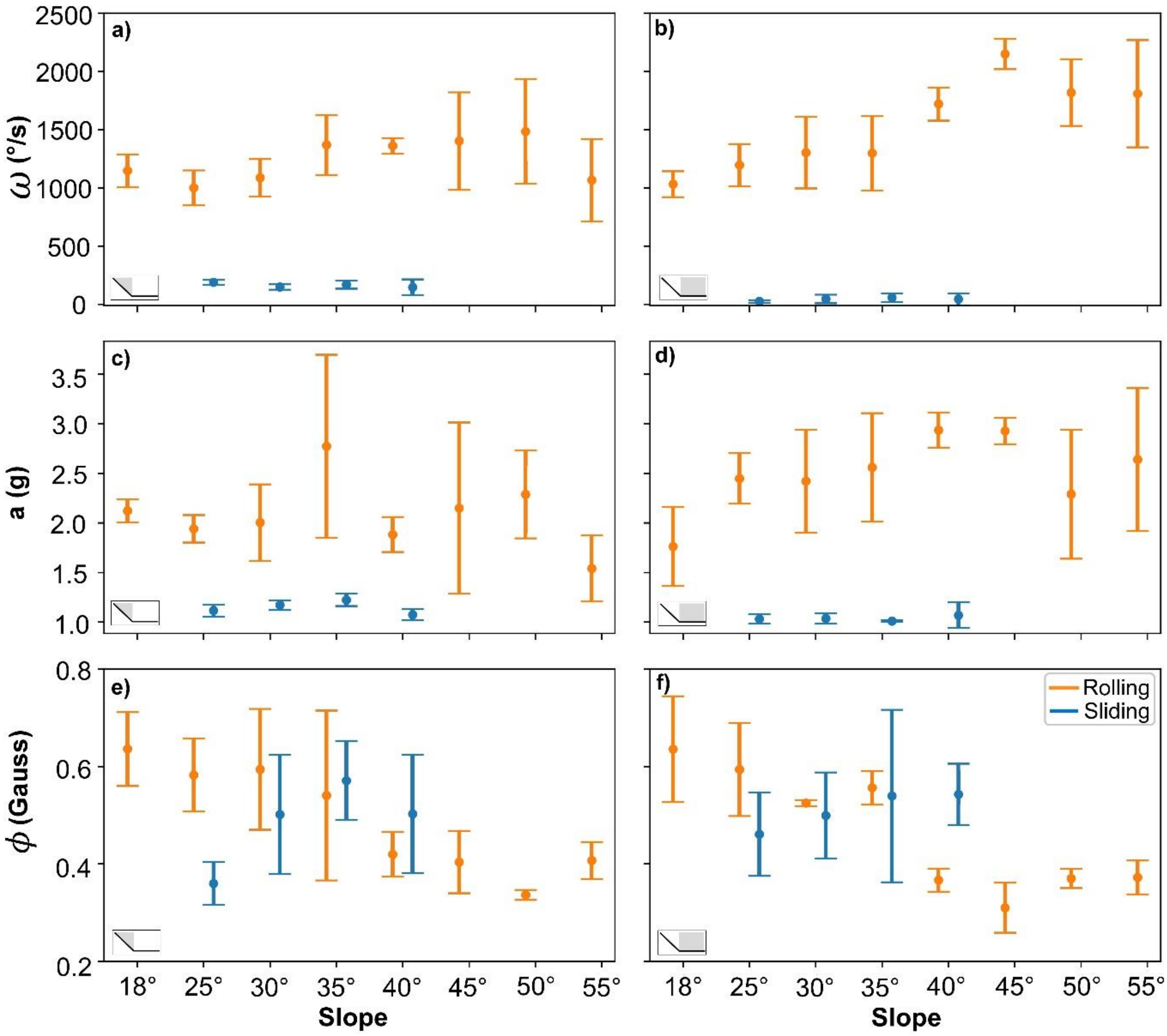

Figure 6. Lumped representation of cobble motion for rolling and sliding experiments using raw data. (a, c, and e) Error bars for motion on the inclined plane. (b, d, and f) Error bars for the motion on the horizontal plane. The mean magnitude of (a and b) angular velocity, (b and c) acceleration, and (e and f) magnetic field. Amber error bars refer to experiments with a sliding cobble, whereas blue error bars are tests with a rolling cobble.

3.4 Kinetic energy as representation of motion

The total kinetic energy of an object is defined as the sum of the translational and rotational energy (e.g., Díaz, 2019):

$$E_{TOT} = K + R = \frac{1}{2} m v_G^2 + \frac{1}{2} \omega^T I \omega \qquad (1)$$

where m is the mass of the cobble, v_G is the velocity magnitude of the centre of mass, ω is the angular velocity, while I is the moment of inertia of the cobble. By approximating the cobble as a sphere of radius R, the moment of inertia is $\frac{2}{5}mR^2$. The first term on the right-hand side is translational energy, whereas the second term is the rotational energy. Given the mass and the average diameter of the cobble, the variation of the average total kinetic energy can be calculated with respect to the inclination of the slope using the magnitude of linear and angular velocity (Figure 7). The linear velocity is computed through the Kalman filter fed by the camera-based positions and sensor-based linear accelerations (see the Supplementary Material for further details), whereas the angular velocity is inferred from the orientation angles (Section 2.3, Figure 3).

For the rolling experiments, on the inclined plane, the total kinetic energy increases with incline up to 45° (Figure 7e). Then, the energy slightly decreases at 50°and 55°, where the average value stays between 4 J and 6 J. Similarly on the horizontal plane (Figure 7f), the total kinetic energy increases with the slope angle but suddenly decreases when the slope angle reaches 50°- 55°. For sliding experiments, on the inclined plane, the total kinetic energy increases until the slope reaches 35° and then it reduces (Figure 7e). On the horizontal plane, the drop in the total kinetic energy occurs at a slope angle of 35 ° - 40° (Figure 7f). A better understanding of the trend shown by the total kinetic energy is provided by the translational and rotational energy. In rolling experiments, as the slope inclination increases, the rotational energy increases and suddenly drops at 55° both on the inclined and horizontal plane (Figure 7c, d). Translational energy increases monotonically on the horizontal plane (Figure 7b). Conversely, on the inclined plane, the increasing trend of the translational energy is interrupted with sudden drops at 40° and at 50° -55° (Figure 7a). By hitting the horizontal board, the cobble makes small bounces. Consequently, the cobble does not keep a point of contact with the boards while it transits from the tilted board to the horizontal board. The impact dissipates energy leading to its decrease at 50° and 55°. In sliding experiments, the rotational energy is very small so that there is a clear separation between modes of movements on the inclined and horizontal planes (amber and blue error bars in Figure 7c, d). The translational kinetic energy on both planes is lower than in the rolling experiments but has the same trend for slope changes between 30° and 40° (Figure 7a, b). Comparing rolling and sliding tests on the same slope, the average value of the total kinetic energy is slightly larger in the rolling experiments since the rotational energy is higher than in the sliding experiments. Indeed, in sliding experiments, the rotational kinetic energy is approximately constant and smaller than in rolling experiments on the inclined and horizontal planes. The translational kinetic energy in sliding experiments has a trend similar to the rolling experiments but with slightly smaller values.

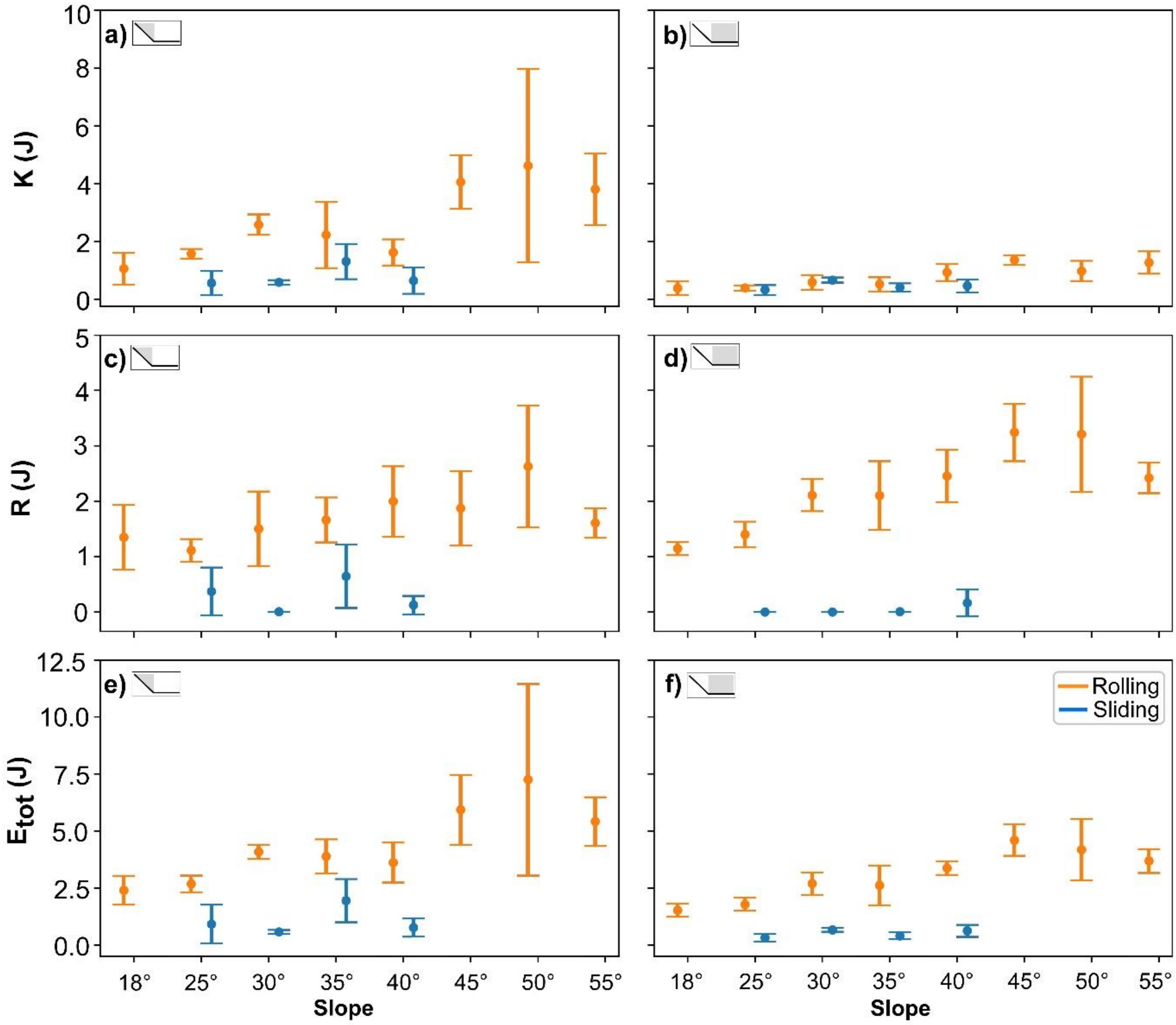

Figure 7. Error bars of (a, b) the mean translational kinetic energy K, (c, d) rotational kinetic energy R and (e, f) total kinetic energy E_{tot} in rolling and sliding experiments. (a, c, and e) Motion on the inclined plane. (b, d, and f) Motion on the horizontal plane. Amber error bars refer to experiments with a sliding cobble, whereas blue error bars describe tests with a rolling cobble (m =0.7 kg; R = 0.05 m; I = 1.68 kg $\cdot$ m^2).

4 Discussion

Our laboratory experiments have given us insights into the possibilities and challenges of smart boulders for landslide monitoring and early warning in field applications. Despite some limitations in the camera and sensor settings dictated by laboratory and design constraints, the protocol and methods developed here are able to provide a lumped representation of the motion magnitude, determine the mode of movement of the cobble and test its signal transmission. Firstly, it seems possible from our experiments with a sand-filled bucket of different depths (section 3.1) to obtain a signal from partially buried sensors, though in a complex field setting this will inevitably also depend on other factors such as geology, topography, atmospheric conditions etc. Preliminary data from field experiments conducted in parallel to our laboratory experiments also suggest that this is the case, with signal obtained even from partially buried sensors (Roskilly et al. 2023; Newby et al., 2024). Laboratory experiments on the style of cobble movement show the potential of IMU sensors for monitoring landslides by detecting the style of movement e.g. by rolling or sliding, and magnitude of movement. Thus, by analysing the activity of boulders distributed on a landslide, it should be possible to analyse landslide movements in time and space. Boulder activity would possibly help to map the boundaries of zones where displacements occur (e.g., Dini et al., 2021) and monitor movement of the underlying landslide. The sensor used in this study is also equipped with a GPS that, although remained deactivated in the laboratory trials, can record the location of the smart boulder outdoors given satellite coverage (Miromico manual, 2020a, b).

Whilst there are benefits of a technology that can move with the landslide over more traditional techniques that may be disrupted by landslide movement, boulders may not remain fully embedded in the body of the landslide for the entire duration of the motion and thus may not always represent underlying landslide movement. The sensor recordings from the field thus need to be carefully analysed to determine whether boulder motion is representative of deeper-seated landslide movement or more surficial movements in flows or rock falls. Moreover, LoRaWAN technology has to provide low-latency data transmission with respect to the timescale of the events being monitored. Thus, the time lag between sensor recording and data retrieval should be carefully studied in field sites. To allow timely data transmission for early-warning system applications, it would be advisable to rapidly characterise the motion of the boulder by computing a high-level metric on-board the sensor (such as the total kinetic energy proposed in this study) and then send this via LoRaWAN with highest priority. A full understanding of landslide behaviour requires monitoring data at different spatio-temporal scales to track local and global movements, correlate movements occurring on the landslide surface and deeper layers and get insight into the sensitivity of subsurface drainage network to rainfall. In the past, an integrated multi-sensor approach has been used to study and frame landslide behaviour (e.g., Castagnetti et al., 2013, Casagli et al., 2017; Wang Z. et al., 2022). Hence, smart boulders could be integrated into a multi-sensor monitoring system where remote-sensing and ground-based measurements are used together to capture fully the landslide behaviour.

5 Conclusions

In view of possible application for monitoring and early warning of landslides, in this study we tested the ability of novel smart sensors to track and characterize cobble motion and send data via wireless network in laboratory experiments~~–~~. Specifically, the study investigated the ability of the sensor to send data via LoRaWAN even when buried in a layer of sand and to detect magnitude and type of motion using the ~~the~~ 9-axis IMU tag. The main experimental findings can be summarised as follows.

First, the Received Signal Strength Indicator (RSSI) declines as the thickness of the sand layer covering the sensor increases. RSSI shows more sensitivity to sand coverage in the magnetometer packets than in the gyroscope and accelerometer packets. Conversely, the Signal-to-Noise Ratio (SNR) stays approximately constant regardless of the sensor. The sensitivity of the LoRaWAN system to possible sand coverage adds a degree of complexity to wireless data transmission in the field and deserves further investigation to better frame the technology potential for landslide monitoring and early warning.

Second, the sensor was able to differentiate between different types of movement of cobbles in our laboratory experiments. Importantly, even without calibration, raw data allows detection of movement and separating two modes of movement, namely rolling, and sliding. This is important because it may be time-consuming and difficult to accurately calibrate sensors used in field-based monitoring systems. In field applications, this finding can potentially be useful to understand the type of motion of the landslide in which smart cobbles/boulders are embedded. However, it is important to consider that raw data do not give reliable values for the acceleration, angular velocity, and magnetic field.

By combining sensor data and camera-based data in the laboratory setting, it was possible to derive a full characterisation of the movements of the cobble. A data fusion approach makes it possible to derive values for position, orientation, velocity, and acceleration allowing the evaluation of the total kinetic energy. As slope increases, the total kinetic energy becomes greater, suggesting its potential use as metric for characterising the cobble motion when embedded in the body of the landslide.

Overall, smart sensors showed their potential to give new insights on the dynamics of complex hazardous flows. In field applications, smart boulders can provide an indication to the initiation of movement and a quantitative approximation of its intensity and could be used effectively to fully capture the landslide behaviour when integrated into a multi-sensor monitoring system.

Notation

$RSSI$	Received Signal Strength Indicator (dBm)
SNR	Signal-to-Noise Ratio (dB)
a	Total acceleration (g)
ω	Angular velocity (°/s)
ϕ	Direction of magnetic field (Gauss)
v_G	Velocity of the centre of mass (m/s)
m	Cobble mass (g)
R	Average cobble radius (m)
I	Moment of inertia (Kg m2)
K	Translational kinetic energy (J)
R	Rotational kinetic energy (J)
E_{tot}	Total kinetic energy (J)

References

AHRS library (2019) AHRS: Attitude and Heading Reference Systems, https://pypi.org/project/AHRS/.

Auflič, M. J., Herrera, G., Mateos, R. M., Poyiadji, E., Quental, L., Severine, B., Peternel, T., Podolszki, L., Calcaterra, S., Kociu, A., Warmuz, B., Jelének, J., Hadjicharalambous, K., Peterson Becher, G., Dashwood, C., Ondrus, P., Minkevičius, V., Todorović, S., Møller, J. J., & Marturia, J. (2023). Landslide monitoring techniques in the Geological Surveys of Europe. Landslides, 20, 951–965. doi: 10.1007/s10346-022-02007-1

Bennett, G. L., Miller, S. R., Roering, J. J., & Schmidt, D. A. (2016). Landslides, threshold slopes, and the survival of relict terrain in the wake of the Mendocino Triple Junction. Geology, 44(5), 363–366. doi: 10.1130/g37530.1

Carlà, T., Intrieri, E., Di Traglia, F., Nolesini, T., Gigli, G., & Casagli, N. (2016). Guidelines on the use of inverse velocity method as a tool for setting alarm thresholds and forecasting landslides and structure collapses. Landslides, 14(2), 517–534. doi:10.1007/s10346-016-0731-5

Casagli, N., Frodella, W., Morelli, S., Tofani, V., Ciampalini, A., Intrieri, E., Raspini, F., Rossi, G., Tanteri, L., & Lu, P. (2017). Spaceborne, UAV and ground-based remote sensing techniques for landslide mapping, monitoring and early warning. Geoenvironmental Disasters, 4(1). doi:10.1186/s40677-017-0073-1

Castagnetti, C., Bertacchini, E., Corsini, A., & Capra, A. (2013). Multi-sensors integrated system for landslide monitoring: critical issues in system setup and data management. European Journal of Remote Sensing, 46(1), 104–124. doi:10.5721/eujrs20134607

Caviezel, A., Schaffner, M., Cavigelli, L., Niklaus, P. S., Bühler, Y., Bartelt, P., Magno, M., & Benini, L. (2018). Design and Evaluation of a Low-Power Sensor Device for Induced Rockfall Experiments. 67(4), 767–779. doi:10.1109/tim.2017.2770799

Caviezel, A., Demmel, S. E., Ringenbach, A., Bühler, Y., Lu, G., Christen, M., Dinneen, C. E., Eberhard, L. A., von Rickenbach, D., & Bartelt, P. (2019). Reconstruction of four-dimensional rockfall trajectories using remote sensing and rock-based accelerometers and gyroscopes. Earth Surface Dynamics, 7(1), 199–210. doi:10.5194/esurf-7-199-2019

Caviezel, A., Ringenbach, A., Demmel, S. E., Dinneen, C. E., Krebs, N., Bühler, Y., Christen, M., Meyrat, G., Stoffel, A., Hafner, E., Eberhard, L. A., Rickenbach, D. von, Simmler, K., Mayer, P., Niklaus, P. S., Birchler, T., Aebi, T., Cavigelli, L., Schaffner, M., & Rickli, S. (2021). The relevance of rock shape over mass—implications for rockfall hazard assessments. Nature Communications, 12(1). doi:10.1038/s41467-021-25794-y

Chang, C., & Wang, G. (2022). Creep of clayey soil induced by elevated pore-water pressure: Implication for forecasting the time of failure of rainfall-triggered landslides. Engineering Geology, 296, 106461. doi: 10.1016/j.enggeo.2021.106461

Clark, M. J. (2023). Monitoring and Characterising Grain Scale Fluvial Bed-load Transport Behaviour using Passive and Active Sensors, PhD Thesis, University of East Anglia. https://ueaeprints.uea.ac.uk/id/eprint/93970/

Crosta, G. B., di Prisco, C., Frattini, P., Frigerio, G., Castellanza, R., & Agliardi, F. (2014). Chasing a complete understanding of the triggering mechanisms of a large rapidly evolving rockslide. Landslides, 11(5), 747–764. doi:10.1007/s10346-013-0433-1

Crosta, G. B., Agliardi, F., Rivolta, C., Alberti, S., & Dei Cas, L. (2017). Long-term evolution and early warning strategies for complex rockslides by real-time monitoring. Landslides, 14(5), 1615–1632. doi:10.1007/s10346-017-0817-8

Coombs, S. P., A. Apostolov, Take, W. A., & J. Benoît. (2020). Mobility of dry granular flows of varying collisional activity quantified by smart rock sensors. Canadian Geotechnical Journal, 57(10), 1484–1496. doi:10.1139/cgj-2018-0278

De Blasio, F. V. (2011). Introduction to the physics of landslides - Lecture notes on the dynamics of mass wasting, Springer Dordrecht, pp. 408. doi: 10.1007/978-94-007-1122-8.

Dewhirst, O. P., Evans, H. K., Roskilly, K., Harvey, R. J., Hubel, T. Y., & Wilson, A. M. (2016). Improving the accuracy of estimates of animal path and travel distance using GPS drift-corrected dead reckoning. Ecology and Evolution, 6(17), 6210–6222. doi:10.1002/ece3.2359

Díaz, E. O. (2019). 3D Motion of Rigid Bodies - A Foundation for Robot Dynamics Analysis. Springer Cham, pp. 474. doi: 10.1007/978-3-030-04275-2

Dini, B., Manconi, A., Loew, S. *and Chophel, J.* (2020). The Punatsangchhu-I dam landslide illuminated by InSAR multitemporal analyses. *Scientific Reports,* 10, 8304, 1-10. doi: 10.1038/s41598-020-65192-w

Dini, B., Bennett, G. L., Franco, A. M. A., Whitworth, M. R. Z., Cook, K. L., Senn, A., & Reynolds, J. M. (2021). Development of smart boulders to monitor mass movements via the Internet of Things: a pilot study in Nepal. Earth Surface Dynamics, 9(2), 295–315. doi:10.5194/esurf-9-295-2021

Dost, J. B., Gronz, O., Casper, M. C., & Krein, A. (2020). The potential of Smartstone probes in landslide experiments: how to read motion data. Natural Hazards and Earth System Sciences, 20(12), 3501–3519. doi:10.5194/nhess-20-3501-2020

Dragino LPS8 manual (2021). LPS8 LoRaWAN Gateway User Manual, Document Version: 1.3.0. https://www.dragino.com/downloads/downloads/LoRa_Gateway/LPS8/LPS8_LoRaWAN_Gateway_User_Manual_v1.3.2.pdf

Feng, D., Shi, Y., Zhao, R., Chen, Y., Zhang, P., Guo, H., & Guo, T. (2023). Study on the mechanism of buffer absorbing energy of double-layer heterostructure based on viscoelastic materials for MEMS devices. Sensors and Actuators a Physical, 364, 114790–114790. doi: 10.1016/j.sna.2023.11479

Ferreira, A. E., Ortiz, F. M., Costa, L. H. M. K., Foubert, B., Amadou, I., & Mitton, N. (2020). A study of the LoRa signal propagation in forest, urban, and suburban environments. Annals of Telecommunications, 75(7-8), 333–351. doi:10.1007/s12243-020-00789-w

Frosio, I., Pedersini, F., & Borghese, N. A. (2009). Autocalibration of MEMS Accelerometers. IEEE Transactions on Instrumentation and Measurement, 58(6), 2034–2041. doi:10.1109/tim.2008.2006137

Gariano, S. L., & Guzzetti, F. (2016). Landslides in a changing climate. Earth-Science Reviews, 162(1), 227–252. doi: 10.1016/j.earscirev.2016.08.011

Gauld, J., Atkinson, P. W., Silva, J. P., Senn, A., & Franco, A. M. A. (2023). Characterisation of a new lightweight LoRaWAN GPS bio-logger and deployment on griffon vultures Gyps fulvus. Animal Biotelemetry, 11(1). doi:10.1186/s40317-023-00329-y

Glueck, M., Oshinubi, D., & Manoli, Y. (2013) Automatic realtime offset calibration of gyroscopes, 2013 IEEE Sensors Applications Symposium Proceedings, Galveston, TX, USA, 214-218, doi:10.1109/SAS.2013.6493589

Goldoni, E., Prando, L., Vizziello, A., Savazzi, P., & Gamba, P. (2018). Experimental data set analysis of RSSI-based indoor and outdoor localization in LoRa networks. Internet Technology Letters, 2(1), e75. doi:10.1002/itl2.75

Goldoni, E., Savazzi, P., Favalli, L., & Vizziello, A. (2022). Correlation between weather and signal strength in LoRaWAN networks: An extensive dataset. Computer Networks, 202, 108627. doi: 10.1016/j.comnet.2021.108627

Gronz, O., Hiller, P. H., Wirtz, S., Becker, K., Iserloh, T., Seeger, M., Brings, C., Aberle, J., Casper, M. C., & Ries, J. B. (2016). Smartstones: A small 9-axis sensor implanted in stones to track their movements. CATENA, 142, 245–251. doi: 10.1016/j.catena.2016.03.030

Guzzetti, F., Gariano, S. L., Peruccacci, S., Brunetti, M. T., Marchesini, I., Rossi, M., Melillo, M. (2020) Geographical landslide early warning systems, Earth-Science Reviews, 200, 102973, 1-29, doi: 10.1016/j.earscirev.2019.102973

Handwerger, A. L., Huang, M.-H., Jones, S. Y., Amatya, P., Kerner, H. R. & Kirschbaum, D. B. (2022). Generating landslide density heatmaps for rapid detection using open-access satellite radar data in Google Earth Engine. Natural Hazards and Earth System Sciences, 22, 753–773. doi: 10.5194/nhess-22-753-2022

Intrieri, E., Carlà, T., & Gigli, G. (2019) Forecasting the time of failure of landslides at slope-scale: A literature review, Earth-Science Reviews, 193(April), 333-349. doi: 10.1016/j.earscirev.2019.03.019

Jeftenić, N., Simić, M., & Stamenković, Z. (2020) Impact of Environmental Parameters on SNR and RSS in LoRaWAN, 2020 International Conference on Electrical, Communication, and Computer Engineering (ICECCE), Istanbul, Turkey, 1-6. doi: 10.1109/ICECCE49384.2020.9179250

Kim, Y., & Bang, H. (2019). Introduction to Kalman filter and its applications. In: F. Govaers, editor, Kalman Filter, chapter 2, 1-17, InTechOpen. doi: 10.5772/intechopen.80600

Lacroix, P., Handwerger, A. L., & Bièvre, G. (2020). Life and death of slow-moving landslides, Nature Reviews Earth and Environment, 1(8), 404-419. doi: 10.1038/s43017-020-0072-8

Le Breton, M., Baillet, L., Larose, E., Rey, E., Benech, P., Jongmans, D., Guyoton, F., & Jaboyedoff, M. (2019). Passive radio-frequency identification ranging, a dense and weather-robust technique for landslide displacement monitoring. 250, 1–10. doi: 10.1016/j.enggeo.2018.12.027

Le Breton, M., Liébault, F., Baillet, L., Charléty, A., Larose, E., & Tedjini, S. (2022). Dense and long-term monitoring of earth surface processes with passive RFID — a review. 234, 104225–104225. doi: 10.1016/j.earscirev.2022.104225

Leinauer, J., Weber, S., Cicoira, A., Beutel, J., & Krautblatter, M. (2023). An approach for prospective forecasting of rock slope failure time. Communications Earth & Environment, 4(1). doi: 10.1038/s43247-023-00909-z

Madgwick, S. O. H., Harrison, A. J. L., & Vaidyanathan, R. (2011). Estimation of IMU and MARG orientation using a gradient descent algorithm, IEEE International Conference on Rehabilitation Robotics, 1-7. doi:10.1109/ICORR.2011.5975346.

Mahony, R., Hamel, T., Morin, P., & Malis, E. (2012). Nonlinear complementary filters on the special linear group. International Journal of Control, 85(10), 1557–1573. doi: 10.1080/00207179.2012.693951

Makris, S., Manzella, I., & Sgarabotto, A. (2024). Scale-dependent processes and runout in bidisperse granular flows: Insights from laboratory experiments and implications for rock/debris avalanches. Journal of Geophysical Research: Earth Surface, 129(9), 1-23. doi: 10.1029/2023JF007469

Maniatis, G. (2021). On the use of IMU (inertial measurement unit) sensors in geomorphology, Earth Surface Processes and Landforms, 46(11), 2136-2140. doi: 10.1002/esp.5197

Manzella, I., Penna, I., Kelfoun, K., & Jaboyedoff, M. (2016) High-mobility of unconstrained rock avalanches: Numerical simulations of a laboratory experiment and an Argentinian event. In: Aversa, S., Cascini, L., Picarelli, L., and Scavia, C. (eds.), Landslides and Engineered Slopes: Experience, Theory and Practice, Proceedings of the 12th International Symposium on Landslides (Napoli, Italy, 12-19 June 2016), 1345-1352. doi: 10.1201/b21520-164

Mao, F., Khamis, K., Krause, S., Clark, J., & Hannah, D. M. (2019). Low-Cost Environmental Sensor Networks: Recent Advances and Future Directions. Frontiers in Earth Science, 7. doi: 10.3389/feart.2019.00221

Miromico AG (2020a) GPS Tracker AT Interface. Miromico AG, Gallusstrasse 4, 8006 Zürich, Switzerland. version 5.3.7.

Miromico AG (2020b) GPS Tracker Application Note - Gyroscope Sampling. Miromico AG, Gallusstrasse 4, 8006 Zürich, Switzerland. version 5.3.11.

Mondini, A. C., Fausto Guzzetti, F., Chang, K.-T., Monserrat, O., Martha, T. R., & Manconi, A. (2021). Landslide failures detection and mapping using Synthetic Aperture Radar: Past, present and future. Earth-Science Reviews, 216, 103574, 1-33. doi: 10.1016/j.earscirev.2021.103574

Newby, K., Bennett, G., Roskilly, K., Sgarabotto, A., Luo, C., & Manzella, I. (2024). Smart boulders for real-time detection of hazardous movement on landslides, EGU General Assembly 2024, Vienna, Austria, 14–19 Apr 2024, EGU24-394. doi: 10.5194/egusphere-egu24-394

Niklaus, P., Birchler, T., Aebi, T., Schaffner, M., L. Cavigelli, A. Caviezel, Magno, M., & Benini, L. (2017). StoneNode: A low-power sensor device for induced rockfall experiments. Repository for Publications and Research Data (ETH Zurich), 1–6. doi:10.1109/sas.2017.7894081

Peng, J., Chen, D., Hassan, M. A., Georgios Maniatis, G., Wang, L. & Nie, R. (2024). Experiments on kinematic characteristics and energy dissipation in rockfall movement on a slope. Physics of Fluids 36, 106625, 1-19. https://doi.org/10.1063/5.0211417

Pollock, W., & Wartman, J. (2020) Human vulnerability to landslides, GeoHealth, 4, e2020GH000287, 1-17. doi: 10.1029/2020GH000287

Roskilly, K., Bennett, G., Curtis, R., Egedusevic, M., Jones, J., Whitworth, M., Dini, B., Luo, C., Manzella, I., & Franco, A. (2022). SENSUM project, Smart SENSing of landscapes Undergoing hazardous hydrogeomorphic Movement, EGU General Assembly 2022, Vienna, Austria, 23-27 May 2022, EGU22-10289. doi:10.5194/egusphere-egu22-10289

Roskilly, K., Bennett, G., Clark, M., Franco, A., Egedusevic, M., Curtis, R., Jones, J., Whitworth, M., Luo, C., & Manzella, I. (2023). Smart cobbles and boulders for monitoring movement in rivers and on hillslopes, EGU General Assembly 2023, Vienna, Austria, 24-28 Apr 2023, EGU23-14870, doi:10.5194/egusphere-egu23-14870

Savazzi, P., Goldoni, E., Vizziello, A., Favalli, L., & Gamba, P. (2019). A Wiener-Based RSSI Localization Algorithm Exploiting Modulation Diversity in LoRa Networks. IEEE Sensors Journal, 19(24), 12381–12388. doi: 10.1109/jsen.2019.2936764

Shobe, C. M., Bennett, G. L., Tucker, G. E., Roback, K., Miller, S. R., & Roering, J. J. (2020). Boulders as a lithologic control on river and landscape response to tectonic forcing at the Mendocino triple junction. GSA Bulletin, 133(3-4), 647–662. doi: 10.1130/b35385.1

Shobe, C. M., Turowski, J. M., Nativ, R., Glade, R. C., Bennett, G. L., & Dini, B. (2021). The role of infrequently mobile boulders in modulating landscape evolution and geomorphic hazards. Earth-Science Reviews, 220, 103717. doi: 10.1016/j.earscirev.2021.103717

Sim, K. B., Lee, M. L., & Wong, S. Y. (2022). A review of landslide acceptable risk and tolerable risk. Geoenvironmental Disasters, 9(1). doi: 10.1186/s40677-022-00205-6

Soriano-Redondo, A., Franco, A. M. A., Acácio, M., Martins, B. H., Moreira, F., & Catry, I. (2021). Flying the extra mile pays-off: Foraging on anthropogenic waste as a time and energy-saving strategy in a generalist bird. Science of the Total Environment, 782, 146843. doi: 10.1016/j.scitotenv.2021.146843

Souza, B., & Benoît, J. (2024). Rockfall motion using a Smart Rock sensor. Canadian Geotechnical Journal, 61(4), 802–819. doi: 10.1139/cgj-2022-0599

Wang, C., Guo, W., Yang, K., Wang, X., & Meng, Q. (2022). Real-Time Monitoring System of Landslide Based on LoRa Architecture. Frontiers in Earth Science, 10. doi: 10.3389/feart.2022.899509

Wang, Z., Hu, J., Chen, Y., Liu, X., Liu, J., Wu, W., & Wang, Y. (2022). Integration of ground-based and space-borne radar observations for three-dimensional deformations reconstruction: application to

Luanchuan mining area, China. Geomatics, Natural Hazards and Risk, 13(1), 2819–2839. doi: 10.1080/19475705.2022.2134828

Further references mentioned in the Supplementary material

Bradski, G. (2000) The OpenCV Library. Dr. Dobb's Journal of Software Tools, 120, 122-125.

Liu, L., Ouyang, W., Wang, X., Fieguth, P., Chen, J., Liu, X., & Pietikäinen, M. (2020). Deep Learning for Generic Object Detection: A Survey. International Journal of Computer Vision, 128(2), 261–318. doi:10.1007/s11263-019-01247-4

Redmon, J., Santosh, D., Girshick, R., & Farhadi, A. (2016). You Only Look Once: Unified, Real-Time Object Detection. ArXiv (Cornell University). doi:10.48550/arxiv.1506.02640

Soeleman, M. A., Hariadi, M., and Purnomo, M. H. (2012). Adaptive threshold for background subtraction in moving object detection using Fuzzy C-Means clustering, TENCON 2012 IEEE Region 10 Conference, Cebu, Philippines, 1-5. doi:10.1109/TENCON.2012.6412265

Soleimanitaleb, Z., Keyvanrad, M. A., and Jafari, A. (2019) Object Tracking Methods: A Review, 9th International Conference on Computer and Knowledge Engineering (ICCKE), Mashhad, Iran, 282-288. doi: 10.1109/ICCKE48569.2019.8964761.

Stolle, J., Nistor, I., & Goseberg, N. (2016). Optical Tracking of Floating Shipping Containers in a High-Velocity Flow. Coastal Engineering Journal, 58(2), 1650005–16500011650005–1650029. doi: 10.1142/s0578563416500054

Zhang, Z. (2000). A flexible new technique for camera calibration, IEEE Transactions on Pattern Analysis and Machine Intelligence, 22(11), 1330-1334. doi: 10.1109/34.88871.